LASER & PHOTONICS REVIEWS
www.lpr-journal.org

Broadband Asymmetric Light Transport in Compact Lithium Niobate Waveguides

Shengjie Wu, Wange Song, Jiacheng Sun, Zhiyuan Lin, Haoran Xin, Shining Zhu, and Tao Li**

Asymmetric on-chip light transport is important but always challenging for photonic integrations. Although it has been recently implemented by adiabatically encircling the exceptional points in a non-Hermitian system, these approaches are fundamentally restricted to the adiabatic condition that brings disadvantages of low transmission efficiency and large device footprint. Here, it is proposed to realize a broadband asymmetric light transport in compact non-Hermitian coupled waveguides on the lithium niobate-on-insulator (LNOI) platform. The asymmetric function is fulfilled by a particular mode selection in a loss-controlled LNOI waveguide triplet, where a lossless zero mode plays a crucial role. Moreover, the shortcut to adiabaticity is applied to speed up the light evolution and shorten the device length. The approach works out a new strategy to establish an asymmetric light transport in a compact form, indicating further new on-chip light manipulations in this promising LNOI photonic platform.

1. Introduction

Non-Hermitian (NH) photonics with tailored gain and loss promises intriguing light behaviors and functional devices. In a non-Hermitian system with parity-time symmetry, two or more eigenvalues and eigenstates degenerate simultaneously at the exceptional point (EP), which is the origin of exotic phenomena that have no Hermitian counterparts.[1–8] By adiabatically encircling an EP in non-Hermitian arrangements of waveguides, chiral asymmetric light transmission has been realized,[9–16] and functional devices have been developed, such as asymmetric mode converter[9,10,13,19] and chiral polarizer.[15,18] Benefited from the adiabatic process, reported devices show robust and broadband properties. However, the fundamental adiabatic condition in such protocol requires slow encirclement in the lossy system and inevitably leads to large device size and low transmission efficiency.[9,12,13] Great efforts have been made to achieve efficient and compact asymmetric integrated devices, such as the Hamiltonian hopping protocol for fast EP encirclement,[17–19] while it is still challenging to improve their comprehensive performance to meet the requirement for compact photonic integrations.

As a new integrated-photonics platform, lithium niobate-on-insulator (LNOI) enables promising functionalities due to its excellent optical properties.[20–26] Although EP encircling strategy to access the on-chip asymmetric light behaviors has been demonstrated in integrated silicon platform,[12,14–19] it is never successfully employed in the LNOI platform. A major obstacle would attribute to the lower field confinement of LN waveguides that will lead to extremely long light propagations in the EP encircling process and make the whole device unacceptably large for integration. Besides, the non-Hermitian loss modulation on LNOI is rarely explored before and the device performance may be further degraded due to the lower refractive index contrast in LNOI, thus making it difficult to directly transplant the existing schemes of asymmetric light manipulation into the LNOI platform. Therefore, it is necessary to develop a new strategy to work for the LNOI chip.

Fortunately, the shortcut to adiabaticity (STA) technique is proposed in quantum physics to speed up the quantum state transfer.[27–30] In the STA-designed system, the diabatic transition in the fast evolution process is suppressed and the system evolves exactly following the adiabatic reference, thus producing the same final state as the adiabatic process in a shorter time/length. The STA protocol can also be introduced to photonic systems,[31–33] where the light evolution can be significantly speeded up through a nonadiabatic route, making it promising for efficient and compact light manipulation.

In this paper, we theoretically propose and experimentally demonstrate a broadband asymmetric light transport in a compact LNOI platform with STA-designed non-Hermitian coupled waveguides (NHCW). The non-Hermitian modulation is created by depositing the loss element (i.e., chromium strip) on top of the LN waveguide, which gives rise to asymmetric light behavior by a selective mode dissipation. For the forward transport, the light field bypasses the loss element through a lossless zero mode, which gives rise to full light transport with mode conversion. For the backward, the interplay of eigenmodes and loss modulation

S. Wu, W. Song, J. Sun, Z. Lin, H. Xin, S. Zhu, T. Li
National Laboratory of Solid State Microstructures, Key Laboratory of Intelligent Optical Sensing and Manipulations
Jiangsu Key Laboratory of Artificial Functional Materials
College of Engineering and Applied Sciences
Nanjing University
Nanjing 210093, China
E-mail: songwange@nju.edu.cn; taoli@nju.edu.cn

The ORCID identification number(s) for the author(s) of this article can be found under https://doi.org/10.1002/lpor.202300306

DOI: 10.1002/lpor.202300306

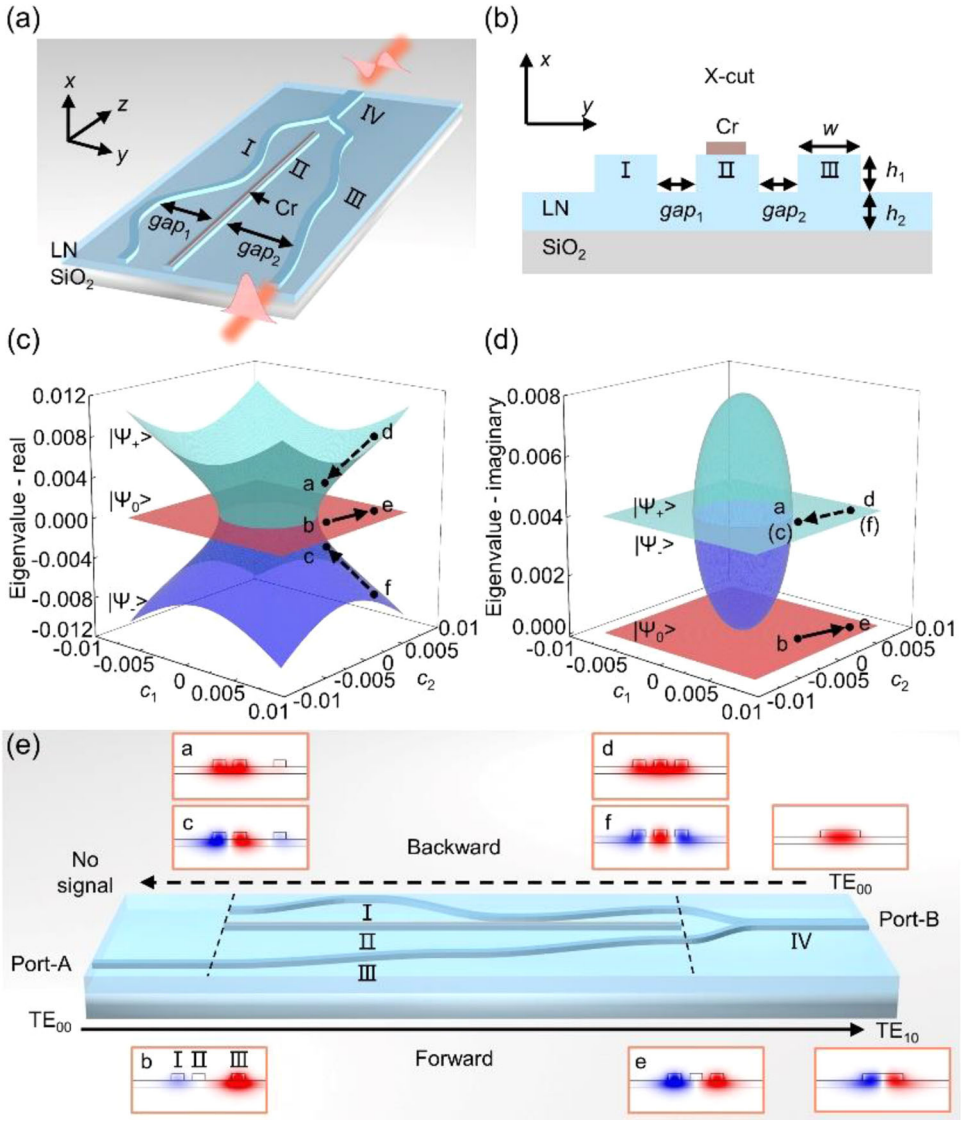

Figure 1. Design of the NHCW for asymmetric light propagation. a) Schematics of the waveguide system for asymmetric light transport on the X-cut LNOI platform, consisting of the NHCW (I, II, and III) and a multimode waveguide (IV) connected by a Y-branch. The gray strip on top of the central waveguide corresponds to the chromium (Cr) to create the non-Hermitian potential. b) Cross-section of the coupled waveguides I-III. The parameters of each ridge waveguide are $w = 600$ nm, $h_1 = 300$ nm, and $h_2 = 300$ nm. c,d) Real and imaginary parts of the band structures. The cyan and blue branch correspond to split modes $|\Psi_+>$ and $|\Psi_->$, and the red one is the zero mode $|\Psi_0>$. The mode evolution paths associated with forward and backward passage are indicated by solid and dashed arrows, respectively. e) Asymmetric light transport and associated eigenstate mode profile. In the forward case (bottom), TE_{00} input from Port-A evolves along $|\Psi_0>$, which bypasses the loss element and converts to TE_{10} at Port-B. In the backward case (top), TE_{00} input from Port-B excites lossy $|\Psi_+>$ and $|\Psi_->$. No signal comes out from Port-A due to high dissipation.

completely forbids the transmission. Our experiments show a high contrast ratio for the forward and backward light transportations with robust and broadband properties, agreeing well with the theoretical expectation. Different from previous works with inevitable lossy mode engaged in the EP encircling,[9–12,14,17–19] our NHCW supports lossless and symmetry-protected supermode that indeed accounts for high-efficiency transmission. Importantly, our STA design in NHCW significantly reduces the size of the functional device, which would enable more integration in the LNOI platform efficiently.

2. Results

2.1. Asymmetric Light Transfer with Non-Hermitian LNOI Waveguide Triplet

The scheme of the asymmetric light transport device on the LNOI platform is shown in **Figure 1**a,b, which consists of three coupled single-mode waveguides (I, II, and III) and a multimode waveguide (IV). The waveguide-IV is connected to waveguide -I and -III through a Y-branch. The waveguide-II is straight and has a

chromium (Cr) strip on the top, creating the non-Hermitian potential, and waveguide-I and -III follow arbitrary trajectories that modulate the coupling between waveguides. The NHCW system can be described by the following Hamiltonian according to the coupled mode theory (CMT)[6,7]

$$H_0(z) = \begin{bmatrix} \beta & c_1(z) & 0 \\ c_1(z) & \beta + i\gamma & c_2(z) \\ 0 & c_2(z) & \beta \end{bmatrix} \quad (1)$$

where z is the propagation direction, β is the propagation constant, and γ donates the loss. $c_1(z)$ and $c_2(z)$ are the z-dependent coupling coefficients between adjacent waveguides.

The band structure of the NHCW with respect to coupling coefficients c_1 and c_2 can be calculated by CMT, which consists of two split modes $|\Psi_+>$ and $|\Psi_->$ (cyan and blue branches in Figure 1c,d) with

$$\beta_\pm = \beta + i\frac{\gamma}{2} \pm \frac{1}{2}\sqrt{4(c_1^2 + c_2^2) - \gamma^2} \quad (2)$$

and one zero mode $|\Psi_0>$ (red branch) with $\beta_0 = \beta$. There is a continuous closed trajectory [following $4({c_1}^2+{c_2}^2) = \gamma^2$] on the c_1-c_2 plane, at which the real and imaginary parts of the eigenvalues $\beta_\pm$ are identical. This circled trajectory is an exceptional ring.[34,35] Both split modes ($|\Psi_+>$ and $|\Psi_->$) are dissipative with nonzero imaginary part in all c_1-c_2 region (see Figure 1d, cyan and blue branches). In contrast, the zero mode is always pinned at zero energy regardless of the c_1 and c_2 (see the red flat plane in Figure 1c), indicating the robustness of this mode, which is protected by the chiral symmetry.[6,36,37] More importantly, attributed to the antisymmetric mode profile on side waveguides and no energy on the central one (see mode-e in Figure 1e; and Equations S1–S3 in the Supporting Information), the zero mode is lossless regardless of the loss γ implemented on the central waveguide (see Figure 1d, red plane).

Similar to the chiral mode switching via encircling EP,[9–19] asymmetric light transport can be realized in our structure by a non-Hermitian mode selection. Here, waveguides-III and -IV are extended as input/output (Port-A and Port-B), respectively. The corresponding mode evolution in the triplet for the forward and backward propagations are indicated by arrows (solid arrow for the forward case, and dashed arrow for the backward case) and the associated eigenstates at Port-A (marked by a, b, and c) and Port-B (marked by d, e, and f) are shown in Figure 1e. In the forward case, fundamental TE_{00} mode is input from Port-A and excites the zero mode $|\Psi_0>$ (mode-b) due to large field overlap, which evolves to the profile of mode-e along the zero mode, as shown in Figure 1e. The corresponding evolution trajectory in the band structure is also marked (see solid arrow in Figure 1c,d). This antisymmetric mode profile of mode-e could excite the TE_{10} mode in the multimode waveguide IV (Figure 1e bottom right). Since the lossy central waveguide does not implement any dissipation on the zero mode, efficient and low-loss passage is obtained in the forward case. In contrast, when the fundamental TE_{00} mode is input from Port-B in the backward case (Figure 1e top), the symmetric TE_{00} mode in waveguide IV cannot excite the antisymmetric zero mode in the NHCW (I-III). Instead, split modes $|\Psi_+>$ and $|\Psi_->$ are excited (mode-d and -f), which have symmetric mode profiles on waveguide-I and -III. Both split modes adiabatically evolve along the trajectories indicated by dashed arrows ($|\Psi_+>$ from mode-d to a, and $|\Psi_->$ from mode-f to c). It is clearly shown in Figure 1d that these two evolution paths experience significant loss (the imaginary part is nonzero), thus the backward signal cannot pass this device due to energy dissipation. In short, by utilizing the lossless zero mode in the forward passage and two lossy split modes in the backward passage, the asymmetric light transport effect can be realized.

2.2. Shortcut to Adiabaticity Strategy

The aforementioned process usually requires adiabatic conditions, i.e., the structure parameters should evolve slowly to avoid mode crosstalk, which inevitably enlarges the device footprint. To realize the mode transfer in a more compact device, we apply the shortcut to adiabaticity (STA) to accelerate the mode evolution. First proposed by M. Berry,[27] the transitionless driving is a kind of STA method that can suppress the instantaneous eigenmode coupling induced by fast parameter manipulation via adding counterdiabatic driving terms.[27–31,33] The transitionless driving method has been adopted in quantum systems to speed up the state evolution,[29,30] but it requires complex coupling modulation (i.e., both real and imaginary coupling) and induces long-range couplings,[29] which are difficult to be implemented in LNOI-coupled waveguides. Here, we circumvent the difficulty by the following steps: First, we have noticed that the original Hamiltonian $H_0(z)$ satisfies the so-called one-photon resonance condition (i.e., the mode constants of waveguides I-III are equal), which allows one to map the three-level system $H_0(z)$ to an effective two-level one $H_{\text{eff}}(z) = \begin{bmatrix} c_2(z)/2 & c_1(z)/2 \\ c_1(z)/2 & -c_2(z)/2 \end{bmatrix}$ (refs. [28, 32]). Then, the counterdiabatic driving term $H_{\text{eff\_CD}}(z)$ for $H_{\text{eff}}(z)$ is designed by following Berry's protocol[27]

$$H_{\text{eff\_CD}}(z) = i\sum_n \sum_{m\neq n} \frac{|m(z)\rangle\langle m(z)|\frac{\partial}{\partial z}H_{\text{eff}}(z)|n(z)\rangle\langle n(z)|}{E_n(z) - E_m(z)} \quad (3)$$

Here, $H_{\text{eff\_CD}}(z)$ suppresses the diabatic eigenmode transfer of fast varying $H_{\text{eff}}(z)$, and the STA Hamiltonian $H_{\text{eff\_STA}}(z)$ is obtained by adding $H_{\text{eff}}(z)$ and $H_{\text{eff\_CD}}(z)$. Finally, the STA version of the coupled waveguides I-III $H_{\text{STA}}(z)$ is obtained by mapping $H_{\text{eff\_STA}}(z)$ back to a three-level system, which is described by

$$H_{\text{STA}}(z) = \begin{bmatrix} \beta & \tilde{c}_1(z) & 0 \\ \tilde{c}_1(z) & \beta & \tilde{c}_2(z) \\ 0 & \tilde{c}_2(z) & \beta \end{bmatrix} \quad (4)$$

This new Hamiltonian can be implemented in LNOI waveguide systems by varying the waveguide gaps along the propagation direction (z direction in our case), as the scheme shown in Figure 1a,e. The waveguide width holds constant, and gap_1 and gap_2 are designed so that the coupling strength $\tilde{c}_1(z)$ and $\tilde{c}_2(z)$ fulfill the STA Hamiltonian H_{STA} (see the Supporting Information for design details).

Figure 2a shows the scheme of state evolution in an adiabatic system (left), a fast-modulated nonadiabatic system (middle) and an STA system (right). In the adiabatic system with a long length

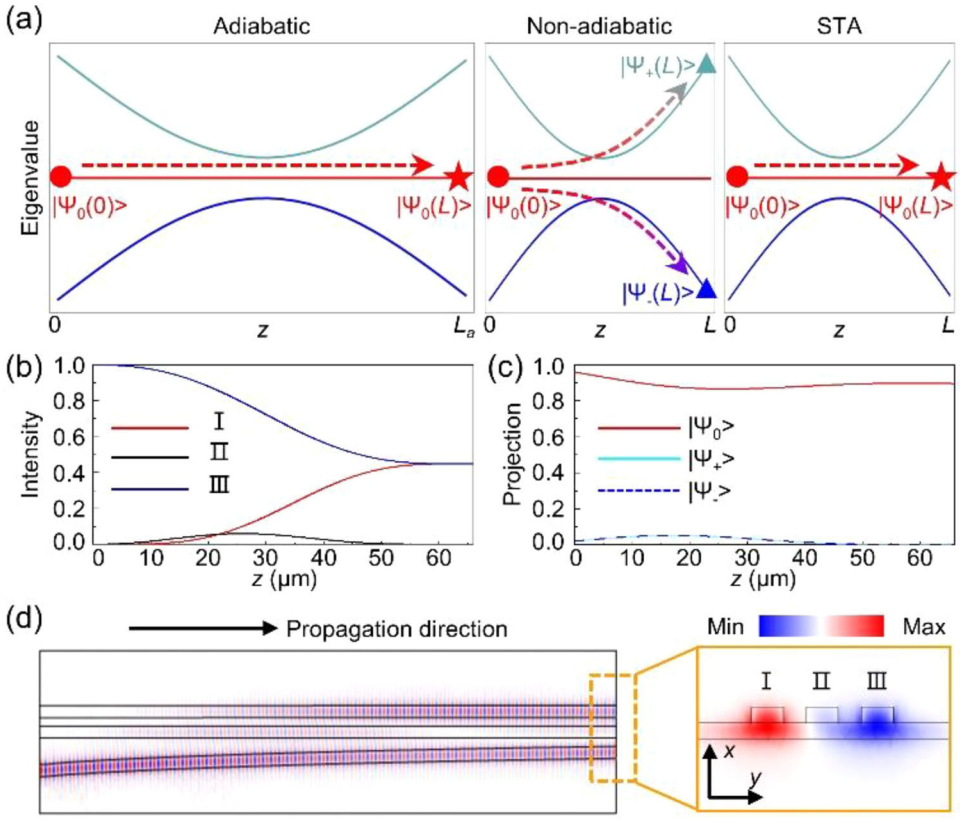

Figure 2. Optical field evolution in the STA-designed NHCW. a) Schematics of the light evolution trajectory in the adiabatic system with long length L_a (left), nonadiabatic system by directly shortening the adiabatic system to a shorter length L (middle) and STA designed system with the same shorter length L (right). The red disk and red pentagrams correspond to the zero mode at Port-A ($|\Psi_0(0)>$) and Port-B ($|\Psi_0(L)>$), respectively. The green and blue triangles correspond to two split modes ($|\Psi_+(L)>$ and $|\Psi_-(L)>$) at Port-B. b) CMT calculated evolution of light intensity with light input from waveguide III. Light field comes out from side waveguides with equal intensity. c) Projection of the light field onto instantaneous eigenstates. The zero mode $|\Psi_0>$ overwhelms the split modes $|\Psi_+>$ and $|\Psi_->$, all along the propagation. d) Simulated optical field evolution (E_y component) in the forward propagation and the output field in the structure.

L_a (usually several hundred micrometers[12]), the adiabatic condition is satisfied and the input mode always stays exactly on its own eigenmode. In the nonadiabatic system, a simple reduction in the device length would break the adiabatic condition and result in significant eigenmode crosstalk between initially excited zero mode $|\Psi_0>$ and two split modes $|\Psi_\pm>$. In the STA case, the counterdiabatic driving terms effectively suppress the unwanted mode coupling and pin the light field on the evolution trajectory of the zero mode $|\Psi_0(z)>$ even in a fast-varying system. The CMT calculated field evolution in the STA-designed structure with light injected into waveguide III is depicted in Figure 2b,c. The zero mode is significantly excited due to the large overlap between its mode field and input light field. The light field comes out from the waveguide I and III with equal intensity, as shown in Figure 2b. Attributed to the counterdiabatic driving, coupling among instantaneous eigenmodes is suppressed, thus the dominant eigenmode is the zero mode all along the propagation. This can be seen from the projection of the light field to instantaneous eigenstates shown in Figure 2c.

Furthermore, we carried out full-wave simulations on this STA-designed non-Hermitian LN structure. The width w and height h_1 of the LN waveguides are 600 and 300 nm, respectively, in which only one fundamental TE_{00} mode is supported with propagation constant $\beta_0 = 1.87k_0$ at $\lambda = 1550$ nm. The waveguide bending profile is carefully designed to make the coupling coefficients fulfill the corresponding STA Hamiltonian. We introduce non-Hermitian loss modulation with a field attenuation coefficient of $\gamma = 0.008\ k_0$ to the central waveguide. The length of NHCW is 66 μm. Figure 2d shows the simulated electric field (E_y) evolution in the coupled waveguides and the inset depicts the E_y field at the output facet of the NHCW I-III, which clearly shows the output field equally distributes on waveguide -I and -III with a π phase difference-a signature of the zero mode.

2.3. Experimental Results

We fabricate the experimental samples on the X-cut LNOI platform according to the simulation parameters. The multimode waveguide-IV has a width of 1200 nm and supports two modes, a fundamental TE_{00} mode ($\beta_{00} = 1.96\ k_0$) and a high-order TE_{10} mode ($\beta_{10} = 1.86\ k_0$). Two grating couplers for couple-in/-out light are connected to waveguides -III and -IV, marked by Port-A and -B, respectively (**Figure 3**a). The non-Hermitian LNOI samples are fabricated using the method of electron beam lithography (EBL) and the dry etching process. A 300 nm wide and 20 nm

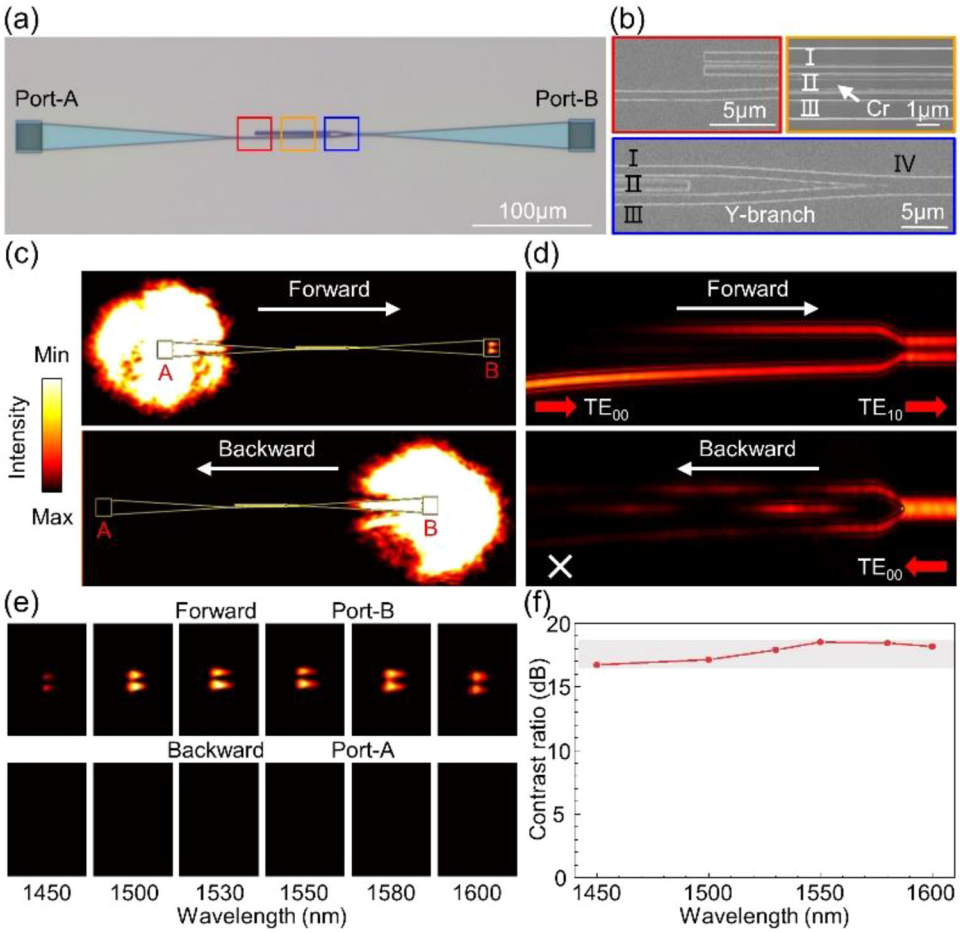

Figure 3. Broadband asymmetric light transport in the STA-designed non-Hermitian LNOI system. a) Optical microscope photograph of the sample. b) Enlarged SEM pictures of the NHCW with Cr strip (top), and the Y-branch connecting waveguides I, III, and multimode waveguide IV (bottom). c) Experimentally recorded asymmetric light output signal in forward (top) and backward transportation (bottom). d) Simulated field evolutions of input TE_{00} mode for forward and backward. e) Charge–coupled device (CCD) captured images of Port-B in the forward case and Port-A in the backward case with different wavelengths. f) Experimentally measured contrast ratios from 1450 to 1600 nm.

thick Cr strip is deposited by a second-step E-beam lithography with the alignment and lift-off process (see the Experimental Section for details). The optical microscope image of the sample and scanning electron microscopy (SEM) images of enlarged structures are shown in Figure 3a,b, where the deposited Cr stripe is distinguishable.

The experimental results and the corresponding simulated light field evolutions are shown in Figure 3c,d, respectively. In the forward case, Port-A couples the focused laser to TE_{00} mode in waveguide III. The lossless zero mode in the NHCW is excited and finally evolves to the TE_{10} mode at Port-B, which is verified by the two bright spots from Port-B in the experimental result (Figure 3c, top) and light field evolution in the numerical simulation (Figure 3d, top). The simulated crosstalk between the output TE_{00} and TE_{10} modes, defined as $20\lg_{10}(I_{00}/I_{10})$, is −41.36 dB, corresponding to ≈99.15% coupling efficiency from TE_{00} to TE_{10} modes, where I_{00} and I_{10} correspond to the output intensity of TE_{00} and TE_{10} mode from Port-B, respectively. In the backward case, TE_{00} mode in waveguide IV is excited by the input laser, which evolves along the two lossy split modes in NHCW. As a result, the light is dissipated and no output signal from Port-A is detected in the experiment (Figure 3c bottom), which agrees well with the simulation result (Figure 3d bottom). The device works as a TE_{00}-TE_{10} mode converter in the forward case and prohibits the signal in the backward case, indicating a significant asymmetric response. To quantify the performance of the asymmetric light transport, the contrast ratio $CR = 20\lg(I_{forward}/I_{backward})$ is defined, where $I_{forward}$ ($I_{backward}$) is output intensity from Port-B (Port-A) in the forward (backward) case. The CR is measured to be ≈18.5 dB at 1550 nm in experiments. Benefiting from the symmetry-protected zero mode, the asymmetric response exists in a broadband. As shown in Figure 3e, the experimentally captured output signals from Port-A and -B for different wavelengths (1450, 1500, 1530, 1550, 1580, and 1600 nm) all demonstrate good asymmetric transports. The measured CR is larger than 16 dB in a wide bandwidth (from 1450 to 1600 nm), indicating good potential in broadband photonic integrations (see Figure 3f).

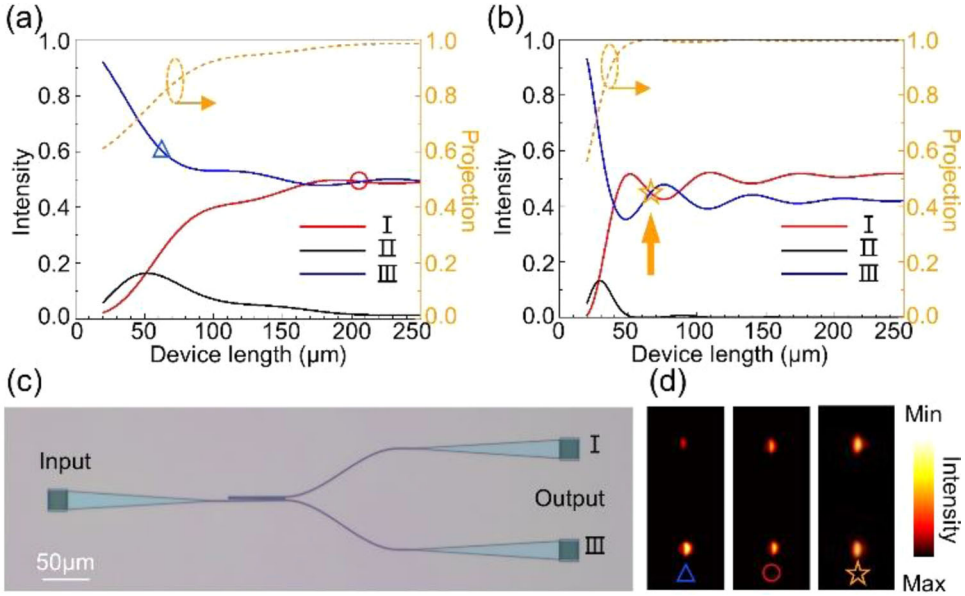

Figure 4. Comparison between adiabatic and STA-designed devices. a,b) CMT calculated output intensity (solid lines) and the projection of output filed to the zero mode (dashed lines) of different device lengths for a) STIRAP- and b) STA-designed structures. c) Optical microscope photograph of the samples. d) Experimental results of the output signals from waveguide -I and -III. Left: $L = 66$ μm (nonadiabatic, blue triangle). Middle: $L = 200$ μm (adiabatic, red circle). Right: $L = 66$ μm (STA, orange pentagram).

3. Discussion and Conclusion

To demonstrate the advantage of the STA strategy, we compare the conventional adiabatic process [e.g., stimulated Raman adiabatic passage (STIRAP)[38–41]] and our STA-designed structures. **Figure 4**a,b shows the output intensity of waveguides I-III (solid lines) and the projection of the output field to zero mode $|\Psi_0>$ (dashed line) in forward propagations with respect to device lengths for STIRAP and STA structure, respectively. For the STIRAP structure, the zero mode slowly overwhelms other modes as the length increases, thus it can only split light equally on waveguide-I and -III for a long length ≈ 200 μm, red circle), and the performance significantly degrades within nonadiabatic short length (e.g., 66 μm, blue triangle). In contrast, the STA design gives rise to equal output intensity on side waveguides for the same short length (≈66 μm, orange pentagram in Figure 4b), since the zero mode can quickly dominate for a short length. In experiments, we fabricated three types of samples (see Figure 4c), corresponding to the cases marked by the blue triangle (nonadiabatic), red circle (adiabatic), and orange pentagram (STA) in Figure 4a,b. The observed outcomes align well with the theoretical predictions that the STA sample can fulfill the function within a short device size (Figure 4d, right), while the STIRAP sample can only work for a long length (Figure 4d, middle) and totally breaks down for a short length (Figure 4d, left). Furthermore, we also compare the STA-designed structure with reported asymmetric devices via EP encircling (see Table S1 in the Supporting Information), which clearly shows the potential of the STA strategy in realizing compact on-chip photonic devices.

In conclusion, we have demonstrated a compact and broadband asymmetric light propagation on a non-Hermitian LNOI platform. This interesting asymmetric propagation is implemented through the selective mode conversion and mode dissipation. Specifically, the TE_{00} mode is converted to TE_{10} mode via a lossless zero mode in the forward, while the TE_{00} is totally blocked in the backward due to the large mode dissipation. We further apply a STA strategy to speed-up the "slow" mode evolutions thus giving rise to much reduced device size. The asymmetric light behavior with high contrast ratio in a broad bandwidth is verified by both simulations and experiments. Comparisons between STA-designed and other schemes clearly indicate the potential of the STA protocol in compact integration. This work develops a new strategy for on-chip asymmetric transport, based on which efficient nonreciprocal devices and tunable integrated devices may be explored by harnessing the nonlinear and electro-optic effect of LN material.[42–44] Our non-Hermitian LNOI platform also provides new degrees of freedom in integrated photonic designs, which paves the way for non-Hermitian light manipulation and suggests new functional devices on the promising LNOI chips.

4. Experimental Section

Sample Fabrication: The experimental samples were fabricated using the method of electron beam lithography (EBL) and the dry etching process, which is followed by a second-step E-beam lithography with the alignment and lift-off process to deposit the Cr stripes. The substrate used here is a 500 μm Si substrate with 600 nm Lithium Niobate deposition. The substrates were cleaned in an ultrasound bath in acetone, isopropyl alcohol (IPA), and DI water for 15 min, respectively, and dried under clean nitrogen flow. The alignment marks were then patterned by EBL (Elionix, ELS-F125), deposition of chromium/gold (5 nm/55 nm) layers, and photoresist liftoff. After that, the waveguide arrays and grating nanostructures were exposed to EBL. The samples were then used to dry etch the Lithium Niobate layer in a 16:1 mixture of Ar and CHF3 plasma and the residual photoresist was stripped off by an oxygen plasma stripper. Next, the chromium structures were fabricated by an alignment E-beam lithography and liftoff process.

The photoresist film was spin coated onto the substrate. After exposing the structure, 20 nm chromium film is deposited using thermal evaporation, then removing the photoresist by soaking in N-methyl-2-pyrrolidone.

Optical Measurement: A telecom-band laser (Fianium-1550-SF) was used to characterize the fabricated sample. The laser beam with its polarization being controlled by a polarizer was focused on the grating coupler A(B) from the substrate side by the Mitutoyo near-infrared (NIR) long-working distance object OF (100×, NA = 0.70, f = 200 mm). The transmitted signal was coupled into free space from the air side via the grating coupler B(A) in the forward (backward) case. The output signal was collected by a NIR imaging object OI (50×, NA = 0.42, f = 200 mm) and imaged on a near-infrared charge-coupled device (CCD) camera (Xenics Xeva-1.7-320).

Supporting Information

Supporting Information is available from the Wiley Online Library or from the author.

Acknowledgements

The work was supported by the National Key R&D Program of China (No. 2022YFA1404301), the National Natural Science Foundation of China (Nos. 12174186, 12204233, 62288101, and 92250304), and the Dengfeng Project B of Nanjing University.

Conflict of Interest

The authors declare no conflict of interest.

Data Availability Statement

The data that support the findings of this study are available from the corresponding author upon reasonable request.

Keywords

asymmetric light transfer, integrated photonics, lithium niobate on insulator, non-Hermitian photonics, shortcut to adiabaticity

Received: April 4, 2023
Revised: June 2, 2023
Published online: June 27, 2023

[1] C. M. Bender, S. Boettcher, *Phys. Rev. Lett.* **1998**, *80*, 5243.
[2] L. Feng, R. El-Ganainy, L. Ge, *Nat. Photonics* **2017**, *11*, 752.
[3] S. K. Özdemir, S. Rotter, F. Nori, L. Yang, *Nat. Mater.* **2019**, *18*, 783.
[4] H. Hodaei, M. A. Miri, M. Heinrich, D. N. Christodoulides, M. Khajavikhan, *Science* **2014**, *346*, 975.
[5] S. Xia, D. Kaltsas, D. Song, I. Komis, J. Xu, A. Szameit, H. Buljan, K. G. Makris, Z. Chen, *Science* **2021**, *372*, 72.
[6] W. Song, W. Sun, C. Chen, Q. Song, S. Xiao, S. Zhu, T. Li, *Phys. Rev. Lett.* **2019**, *123*, 165701.
[7] S. Wu, W. Song, S. Gao, Y. Chen, S. Zhu, T. Li, *Phys. Rev. Res.* **2021**, *3*, 023211.
[8] H. Fan, J. Chen, Z. Zhao, J. Wen, Y. Huang, *ACS Photonics* **2020**, *7*, 3035.
[9] J. Doppler, A. A. Mailybaev, J. Böhm, U. Kuhl, A. Gischik, F. Libisch, T. J. Milburn, P. Rabl, N. Moiseyev, S. Rotter, *Nature* **2016**, *537*, 76.
[10] S. N. Ghosh, Y. D. Chong, *Sci. Rep.* **2016**, *6*, 19837.
[11] A. U. Hassan, B. Zhen, M. Soljačić, M. Khajavikhan, D. N. Christodoulides, *Phys. Rev. Lett.* **2017**, *118*, 093002.
[12] J. W. Yoon, Y. Choi, C. Hahn, G. Kim, S. H. Song, K. Yang, J. Y. Lee, Y. Kim, C. S. Lee, J. K. Shin, H. Lee, P. Berini, *Nature* **2018**, *562*, 86.
[13] X. L. Zhang, T. Jiang, C. T. Chan, *Light: Sci. Appl.* **2019**, *8*, 88.
[14] Q. Liu, S. Li, B. Wang, S. Ke, C. Qin, K. Wang, W. Liu, D. Gao, P. Berini, P. Lu, *Phys. Rev. Lett.* **2020**, *124*, 153903.
[15] Y. Wei, H. Zhou, Y. Chen, Y. Ding, J. Dong, X. Zhang, *Photonics Res.* **2022**, *10*, 76.
[16] Z. Feng, X. Sun, *Phys. Rev. Lett.* **2023**, *129*, 273601.
[17] A. Li, J. Dong, J. Wang, Z. Cheng, J. S. Ho, D. Zhang, J. Wen, X. Zhang, C. T. Chan, A. Alù, C. Qiu, L. Chen, *Phys. Rev. Lett.* **2020**, *125*, 187403.
[18] A. Li, W. Chen, H. Wei, G. Lu, A. Alù, C. Qiu, L. Chen, *Phys. Rev. Lett.* **2022**, *129*, 127401.
[19] X. Shu, A. Li, G. Hu, J. Wang, A. Alù, L. Chen, *Nat. Commun.* **2022**, *13*, 2123.
[20] D. Zhu, L. Shao, M. Yu, R. Cheng, B. Desiatov, C. J. Xin, Y. Hu, J. Holzgrafe, S. Ghosh, A. Shams-Ansari, E. Puma, N. Sinclair, C. Reimer, M. Zhang, M. Lončar, *Adv. Opt. Photonics* **2021**, *13*, 242.
[21] A. Boes, L. Chang, C. Langrock, M. Yu, M. Zhang, Q. Lin, M. Lončar, M. Fejer, J. Bowers, A. Mitchell, *Science* **2023**, *379*, 40.
[22] B. Chen, M. Ren, R. Liu, C. Zhang, Y. Sheng, B. Ma, Z. Li, *Light: Sci. Appl.* **2014**, *3*, e189.
[23] M. Xu, M. He, H. Zhang, J. Jian, Y. Pan, X. Liu, L. Chen, X. Meng, H. Chen, Z. Li, X. Xiao, S. Yu, S. Yu, X. Cai, *Nat. Commun.* **2020**, *11*, 3911.
[24] J. Zhang, J. Ma, M. Parry, M. Cai, R. Camacho-Morales, L. Xu, D. N. Neshev, A. A. Sukhorukov, *Sci. Adv.* **2022**, *8*, eabq4240.
[25] Y. Xue, R. Gan, K. Chen, G. Chen, Z. Ruan, J. Zhang, J. Liu, D. Dai, C. Guo, L. Liu, *Optica* **2022**, *9*, 1131.
[26] Y. Liang, J. Zhou, Z. Liu, H. Zhang, Z. Fang, Y. Zhou, D. Yin, J. Lin, J. Yu, R. Wu, M. Wang, Y. Cheng, *Nanophotonics* **2022**, *11*, 1033.
[27] M. V. Berry, *J. Phys. A* **2009**, *42*, 365303.
[28] D. Guéry-Odelin, A. Ruschhaupt, A. Kiely, E. Torrontegui, S. Martínez-Garaot, J. G. Muga, *Rev. Mod. Phys.* **2019**, *91*, 045001.
[29] Y. Li, X. Chen, *Phys. Rev. A* **2016**, *94*, 063411.
[30] Y. Du, Z. Liang, Y. Li, X. Yue, Q. Lv, W. Huang, X. Chen, H. Yan, S. Zhu, *Nat. Commun.* **2016**, *7*, 12479.
[31] A. K. Taras, A. Tuniz, M. A. Bajwa, V. Ng, J. M. Dawes, C. G. Poulton, C. M. D. Sterke, *Adv. Phys.: X* **2021**, *6*, 1894978.
[32] S. Tseng, *Opt. Lett.* **2014**, *39*, 6600.
[33] W. Huang, Y. Chen, X. Qu, S. Yin, X. Shi, X. Xiong, W. Zhang, Z. Qin, Y. Zhang, *AIP Adv.* **2020**, *10*, 095104.
[34] B. Zhen, C. W. Hsu, Y. Igarashi, L. Lu, I. Kaminer, A. Pick, S. Chua, J. D. Joannopoulos, M. Soljačić, *Nature* **2015**, *525*, 354.
[35] A. Cerjan, S. Huang, M. Wang, K. P. Chen, Y. Chong, M. C. Rechtsman, *Nat. Photonics* **2019**, *13*, 623.
[36] P. Boross, J. K. Asbóth, G. Széchenyi, L. Oroszlány, A. Pályi, *Phys. Rev. B* **2019**, *100*, 045414.
[37] W. Song, S. Wu, Y. Chen, C. Chen, S. Gao, C. Huang, K. Qiu, S. Zhu, T. Li, *Phys. Rev. Appl.* **2022**, *17*, 014039.
[38] N. V. Vitanov, A. A. Rangelov, B. W. Shore, K. Bergmann, *Rev. Mod. Phys.* **2017**, *89*, 015006.
[39] R. Menchon-Enrich, A. Llobera, J. Vila-Planas, V. J. Cadarso, J. Mompart, V. Ahufinger, *Light: Sci. Appl.* **2013**, *2*, e90.
[40] H. P. Chung, K. H. Huang, S. L. Yang, W. K. Chang, C. W. Wu, F. Setzpfandt, T. Pertsch, D. N. Neshev, Y. H. Chen, *Opt. Express* **2015**, *23*, 30641.
[41] T. Lunghi, F. Doutre, A. P. Rambu, M. Bellec, M. P. De Micheli, A. M. Apetrei, O. Alibart, N. Belabas, S. Tascu, S. Tanzilli, *Opt. Express* **2018**, *26*, 27058.
[42] L. Wang, X. Zhang, F. Chen, *Laser Photonics Rev.* **2021**, *15*, 2100409.
[43] F. Ye, Y. Yu, X. Xi, X. Sun, *Laser Photonics Rev.* **2022**, *16*, 2100429.
[44] X. Li, J. Ma, S. Liu, P. Huang, B. Chen, D. Wei, J. Liu, *Light: Sci. Appl.* **2022**, *11*, 317.